

Article

Study on a Simplified Structure of a Two-Stage Grid-Connected Photovoltaic System for Parameter Design Optimization

Fan Xie, Zhenxiong Luo, Dongyuan Qiu *, Bo Zhang, Yanfeng Chen  and Liying Huang

School of Electric Power, South China University of Technology, Guangzhou 510641, China; epfxie@scut.edu.cn (F.X.); 201720113821@mail.scut.edu.cn (Z.L.); epbzhang@scut.edu.cn (B.Z.); eeyfchen@scut.edu.cn (Y.C.); ephly@mail.scut.edu.cn (L.H.)

* Correspondence: epdyqiu@scut.edu.cn; Tel.: +86-020-8711-1764

Received: 4 May 2019; Accepted: 5 June 2019; Published: 8 June 2019



Abstract: Conventional parameter designs of two-stage grid-connected photovoltaic (PV) system relied on its mathematical model of the cascade structure (CS), but the procedure is excessively cumbersome to implement. Besides, for a two-stage converter system, the coupling interaction between the power converters can directly lead to a poor parameter design. To overcome this drawback, this paper uses a simplified structure (SS) of single-phase two-stage grid-connected PV system to better design the parameters of the front-stage dc-dc converter. After establishing the small-signal model for SS and CS in the PV system, the relative eigenvalue sensitivity is used as the criterion for judging the influence of some parameters on the stability of the two structures. The stable boundary of MPPT control parameters is compared and discussed in SS and CS, respectively. In addition, the relationship between the front-stage dc-dc converter and the rear-stage dc-ac inverter is analyzed by the modal participation factor calculated in CS. An experiment is also performed at the end of this paper to further verify the feasibility of using SS to design the parameters of the dc-dc converter in the PV system.

Keywords: simplified structure; dc-dc converter; two-stage PV system; parameter design; stability analysis; dc bus

1. Introduction

Renewable energy sources, such as wind and solar energy, have begun to replace traditional energy sources as the main source of energy supply in many countries. With the decreasing cost of photovoltaic (PV) modules [1] and the growing utilization rate of the PV cells [2], the application of PV systems has greatly expanded. Compared with the centralized inverter for the high-power PV grid-connected system, the micro-inverter has some certain advantages, such as reducing the cost and ensuring working at the maximum power point, for low power distributed grid-connected PV systems. According to the arrangements and structural characteristics of the dc bus, the topology of the micro-inverter can be roughly categorized into three types, namely, a cascade converter with a dc bus, an inverter with a pseudo dc bus, and an inverter without a dc bus [3]. Furthermore, these structures involve various types of converters, including the Boost converter, Buck-Boost converter [4,5], Flyback converter [6], and resonant push-pull dc-dc converter [7]. Power electronic converter is an inherently strong nonlinear system and it presents various nonlinear phenomena [8–10]. Thus, in order to design the circuit parameters and control parameters of the PV system, it is necessary to establish the explicit model and analyze its stability.

At present, the small-signal method is usually employed to establish an effective model to analyze the PV power generation system. Wang et al. [11] introduced the small-signal model of the

photovoltaic power generation system in the island operation mode. In [12], the small-signal model of the multi-machine power system with photovoltaic power station is used to study the influence of the low-frequency oscillation of the PV system. It is pointed out that the accessing location and capacity of PV power plant system seriously affects the damping characteristics of the system. Ref. [13] investigated the influence of inverter controller parameters and photovoltaic array structure on the oscillation frequency and damping ratio in large-scale photovoltaic grid-connected power generation systems. Moreover, the maximum power point tracking (MPPT) control is a research hotspot in photovoltaic systems [14–16].

The two-stage PV system is a typical grid-connected PV system. Since the solar panel often provides low level dc voltage in PV systems [1], the first stage is typically a dc-dc converter for amplifying voltage and extracting electrical energy from the PV array, and the second stage is a dc-ac inverter for delivering electrical energy to the utility grid. Distributed PV grid-connected power generation system can usually be divided into two energy conversion stages, which interact with each other to make them exhibit more complex characteristics than the system with a single stage [17–19].

An observer-model was proposed based on Parker transform to analyze the stability of the single-phase two-stage grid-connected PV system [20], and it can effectively analyze the low-frequency oscillation phenomenon existing on the system. However, cascade structure (CS) is still inseparable from the PV system with dc buses to establish an observer-model. In this case, the coupling relationship between parameters may be difficult to determine [21]. Consequently, it is often complicated to design the parameters of the front-stage dc-dc converter as well as to analyze the stability of the PV system.

To simplify the parameter design of two-stage PV system, this paper uses a simplified structure (SS) to substitute CS for the stability analysis of the front-stage Boost converter. The front-stage converter with boost function, such as Boost converter and Flyback converter, can be used to construct SS for two-stage PV system analysis by replacing the dc bus with a voltage source. This paper uses a Boost converter as the front-stage dc-dc converter to expand the discussion. To obtain the relationship between the two structures in terms of stability, the effectiveness of different parameters in dc-dc converter for SS and CS stability needed to find out, including the capacitance and inductance of the Boost converter and the control parameters of the MPPT controller.

So far, there have been attempted to analyze how the parameters affect dynamic performance. The eigenvalue sensitivity is used to analyze the trend of the system eigenvalues when the controller parameters changed [22]. Furthermore, it is pointed out that the parameters of MPPT controller and inner current control loop seriously affect the stability of the system. In [23], the research focus on the connection between the dc-dc converter and dc bus capacitance in the cascade converter, which has found that the dc bus capacitance has a significant effect on the frequency of the oscillation mode.

This paper is structured as follows. Section 2 describes the mathematics model of proposed SS of two-stage PV system with the small-signal model. In Section 3, relative eigenvalue analysis is employed to study the stability of SS under different MPPT control parameters. And, its dynamics frequency characteristics are described through root locus. In Section 4, the feasibility of SS is verified through comparing the stable boundary of SS with that of CS in different parameter domain of MPPT controller. Furthermore, modal participation factor is introduced to expound the relationship between SS and CS. The experimental result is presented in Section 5, and Section 6 concludes this paper.

2. SS with MPPT Control

The topology illustrated in Figure 1 is based on the traditional cascade structure of two-stage PV system. Considering PV system is actually under the weak grid condition, the LC circuit can be used as the output signal filter [24] and the power grid is equivalent to a voltage source connected with an impedance [25]. The dc-dc conversion stage in Figure 1 uses a Boost converter. Since the dc bus voltage is kept near the rated voltage with the control of the dc-ac inverter [8,26], the output voltage of the dc-dc Boost converter is considered to be constant voltage source in this paper. Based on the criterion that dc bus voltage ripple is kept within a certain control range, SS with MPPT controller is

shown in Figure 2, in which C_{in} and L_b are the input filter capacitor and the energy storage inductance, respectively, and the equivalent series resistance (ESR) of C_{in} is represented by R_{Cin} , R_{Lb} is the winding series resistance of L_b .

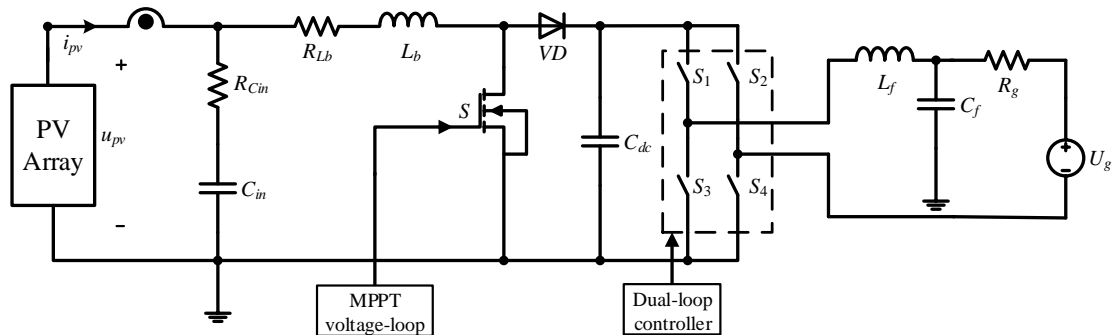


Figure 1. Cascade structure of a Two-Stage Grid-Connected photovoltaic (PV) system.

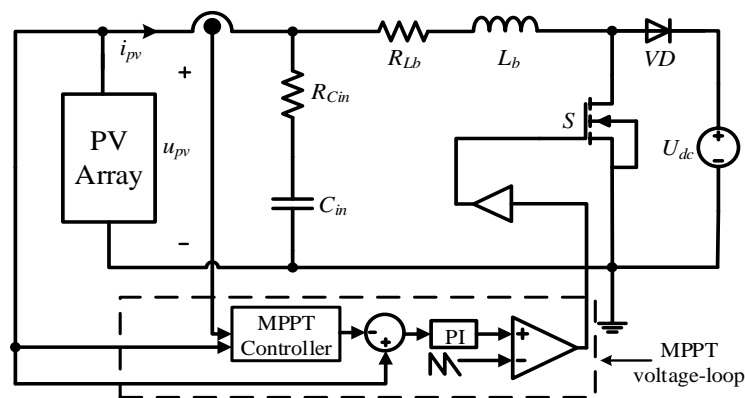


Figure 2. Schematic diagram of simplified structure of Two-Stage Grid-Connected PV system.

To analyze the stability of SS, a suitable mathematical model must be established. Since the parameters of open circuit voltage U_{OC} , short-circuit current I_{SC} , maximum power point voltage U_M and current I_M are usually provided in the data sheet of PV array, the fitting model [27] to describe the nonlinear relationship between PV array output current i_{pv} and voltage u_{pv} are employed in this research. The PV array model can be expressed as

$$i_{pv} = I_{sc} \left(1 - A_1 \left(e^{u_{pv}/(A_2 U_{oc})} - 1 \right) \right) \tag{1}$$

Here, expansion Equation (1) at maximum power point, it can be calculated that $A_1 = \left(1 - \frac{I_M}{I_{sc}} \right) e^{\frac{-U_M}{(A_2 U_{oc})}}$, $A_2 = \left(\frac{U_M}{U_{oc}} - 1 \right) / \ln \left(1 - \frac{I_M}{I_{sc}} \right)$.

Suppose the system is always operating in continuous current mode (CCM). Using the state space averaging method, the averaged equations corresponding to Figure 2 can be derived as follows

$$\begin{cases} u_{pv} = R_{Cin} C_{in} \frac{du_{Cin}}{dt} + u_{Cin} \\ C_{in} \frac{du_{Cin}}{dt} = i_{pv} - i_{Lb} \\ L_b \frac{di_{Lb}}{dt} = u_{pv} - R_{Lb} i_{Lb} - (1 - d_b) U_{dc} \end{cases} \tag{2}$$

where d_b is the duty cycle of the power switch in the dc-dc converter.

Since the applicable scope of the transfer function is defined as a linear time-invariant system, the linearization of Equation (1) at the maximum power point is

$$i_{pv} = -\frac{I_{SC}A_1}{U_{OC}A_2}e^{\frac{U_M}{U_{OC}A_2}}u_{pv} + I_M - \frac{I_{SC}A_1}{U_{OC}A_2}e^{\frac{U_M}{U_{OC}A_2}}U_M \quad (3)$$

Marking the steady state values of u_{Cin} and i_{Lb} at maximum power point as U_{Cin} and I_{Lb} , respectively. Then, adding small signal disturbance to the steady-state value and ignoring the steady-state quantity, Equation (2) can be expressed as follows after performing the Laplace transform.

$$\begin{cases} \hat{u}_{pv}(s) = R_{Cin}C_{in}\hat{u}_{Cin}(s) + \hat{u}_{Cin}(s) \\ C_{in}s\hat{u}_{Cin}(s) = -\frac{I_{SC}A_1}{U_{OC}A_2}e^{\frac{U_M}{U_{OC}A_2}}\hat{u}_{pv}(s) - \hat{i}_{Lb}(s) \\ L_b\hat{i}_{Lb}(s) = \hat{u}_{pv}(s) - R_{Lb}\hat{i}_{Lb}(s) - \hat{d}_b'(s)U_{dc} \end{cases} \quad (4)$$

Here, \hat{u}_{pv} , \hat{u}_{Cin} , \hat{i}_{Lb} , and \hat{d}_b' are all the small disturbance signal.

Thus, the open-loop transfer function from the control input to the PV array output voltage can be derived as

$$G_{vd}(s) = \frac{\hat{u}_{pv}(s)}{\hat{d}_b'(s)} = \frac{sU_{OC}A_2U_{dc}R_{Cin}C_{in} + U_{OC}A_2U_{dc}}{a_2s^2 + a_1s + a_0} \quad (5)$$

where the denominator coefficients are $a_0 = I_{SC}A_1e^{\frac{U_M}{U_{OC}A_2}}R_{Lb} + U_{OC}A_2$, $a_1 = U_{OC}A_2C_{in}R_{Lb} + I_{SC}A_1e^{\frac{U_M}{U_{OC}A_2}}R_{Cin}C_{in}R_{Lb} + I_{SC}A_1e^{\frac{U_M}{U_{OC}A_2}}L_b + U_{OC}A_2R_{Cin}C_{in}$ and $a_2 = U_{OC}A_2C_{in}R_{Lb} + I_{SC}A_1e^{\frac{U_M}{U_{OC}A_2}}R_{Cin}C_{in}R_{Lb}$.

In general, a classical Boost converter using small-signal model in CCM reveals that its $G_{vd}(s)$ contains two real zeros in the S-plane [28]. One is a left half plane zero (LPHZ) due to the parasitic capacitance resistance, another is a right-half-plane zero (RPHZ) being peculiar to Boost topology, which is related to filter inductance, load resistance, and duty cycle. As shown in Equation (5), when the dc bus capacitance can be replaced by a constant voltage source, a stable zero is retained in SS and the RPHZ is eliminated. Since dc-dc Boost converter is connected to a dc-ac inverter in the two-stage PV system, SS is used as the basis of subsequent analysis.

3. Stability Analysis of SS

3.1. Parameter Design

The PV array parameters in SS are shown in Table 1. As usual, the duty cycle d_b is set as 0.5. So, the dc bus rated voltage U_{dc} can be inferred to be 36 V. To meet the requirement both of efficiency and noise interference, the switching frequency f_s of the dc-dc converter is set at 20 kHz.

Table 1. PV Array Parameters.

Parameter	Symbol	Value	Unit
Open-circuit Voltage	U_{oc}	21	V
Short-circuit Current	I_{sc}	1.83	A
Maximum Power Point Voltage	U_M	18	V
Maximum Power Point Current	I_M	1.66	A

The function of the input filter capacitor C_{in} is to reduce the fluctuation of the voltage u_{pv} in the PV array, which improves the output efficiency of the PV array.

The value of the inductor L_b in the Boost converter should be able to ensure that the inductor current ripple is limited to a reasonable range. The inductor current ripple rate is 20%, and the inductance value can be calculated by

$$L_b \geq \frac{d_b(1-d_b)U_{dc}}{f_s \Delta I_{Lb}} = \frac{0.5 \times 0.5 \times 36}{20000 \times 0.2 \times 1.66} \approx 1.36 \text{ mH} \quad (6)$$

this paper takes L_b as 2 mH in consideration of a certain margin.

Furthermore, the ripple of u_{pv} can be expressed as [1]

$$\Delta u_{pv} = \frac{d_b u_{pv}}{4f_s^2 C_{in} L_b} \quad (7)$$

In order to maintain the output power of the photovoltaic cell above 98% of the maximum power, the voltage ripple Δu_{pv} should be less than 8.5% of the maximum power point voltage [29]. Here, we set $\Delta u_{pv} = 0.1\%$ to make SS more accurate in stability analysis as voltage-source replace the bus capacitor, thus obtaining

$$C_{in} \geq \frac{d_b U_M}{4f_s^2 \Delta u_{pv} L_b} = \frac{0.5 \times 18}{4 \times 20000^2 \times 0.001 \times 18 \times 0.002} \approx 156.25 \mu\text{F} \quad (8)$$

C_{in} is taken as 330 μF in consideration of a certain margin.

The parameter value of the proportional integral (PI) controller in the MPPT voltage loop shown in Figure 2 is determined by the Equation (5). With $K_{p1} = 0.11$ and $T_{i1} = 0.01$, the crossover frequency of the open loop f_c is set approximately at 500 Hz, and bode diagram is shown in the Figure 3.

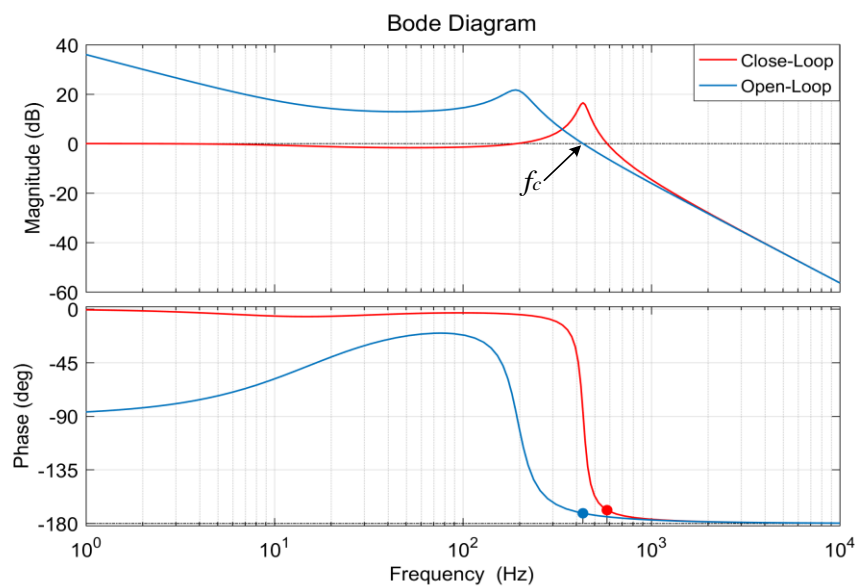


Figure 3. Maximum power point tracking (MPPT) Voltage-Loop Bode Diagram.

3.2. Stability

Let the MPPT controller variable x_{mppt} be

$$\frac{dx_{mppt}}{dt} = u_{pv} - u_{pvref} \quad (9)$$

and duty cycle d_b can be expressed as

$$d_b = K_{p1}(u_{pv} - u_{pvref}) + \frac{K_{p1}}{T_{i1}}x_{mppt} \quad (10)$$

where K_{p1} and T_{i1} are the gain and time constants of PI controller in the MPPT voltage loop, respectively.

The state variable is denoted by $x_{boost} = [u_{Cin}, i_{Lb}, x_{mppt}]^T$. Furthermore, Equations (1), (2), (9), and (10) can be joint to obtain the state-space average model of SS

$$\begin{cases} \frac{du_{Cin}}{dt} = \frac{1}{C_{in}}(I_{sc}(1 - A_1(e^{u_{pv}/(A_2U_{oc})} - 1)) - i_{Lb}) \\ \frac{di_{Lb}}{dt} = \frac{1}{L_b}(u_{pv} - R_b i_{Lb} - (1 - d_b)U_{dc}) \\ \frac{dx_{mppt}}{dt} = u_{pv} - u_{pvref} \end{cases} \quad (11)$$

To study the effect of MPPT controller parameters on the stability of SS, both of R_{Cin} and R_{Lb} are ignored for simplicity. Let the differential term be zero in Equation (11), and the equilibrium point x_e can be obtained. Then, putting Taylor expansion of the state-space average model near x_e and evaluating Equation (12) under first approximation according to Lyapunov method, small-signal model $\frac{d\Delta x_{boost}}{dt} = A_{boost}\Delta x_{boost}$ can be obtained, and

$$A_{boost} = \begin{bmatrix} A_{11} & A_{12} & 0 \\ A_{21} & 0 & A_{23} \\ A_{31} & 0 & 0 \end{bmatrix} \quad (12)$$

is the Jacobian matrix. Where $A_{11} = -\frac{I_{sc}A_1}{C_{in}A_2U_{oc}}e^{\frac{u_{Cin}}{A_2U_{oc}}}$, $A_{12} = -\frac{1}{C_{in}}$, $A_{21} = \frac{1}{L_b} + \frac{U_{dc}K_{p1}}{L_b}$, $A_{23} = \frac{U_{dc}K_{p1}}{L_bT_{i1}}$, $A_{31} = 1$. So, the eigenvalue λ of the small signal model can be solved

$$\det [\lambda \mathbf{I} - A_{boost}] = 0 \quad (13)$$

where \mathbf{I} represent the unit matrix.

It may be noted that, for every value of K_{p1} and T_{i1} , the system contains a real eigenvalue λ_1 and a pair of conjugate eigenvalues $\lambda_{2,3}$, which means it involves one oscillating mode and one attenuation mode. For the eigenvalue of the conjugate complex pair $\sigma \pm j\omega$, the damping ratio of the system oscillation mode can be defined as

$$\xi = \frac{-\sigma}{\sqrt{\sigma^2 + \omega^2}} \quad (14)$$

The indicator ξ can be utilized to characterize the degree of stability of the oscillating mode. To better analyze the influence of the MPPT control parameters on the stability of SS, the eigenvalues and the damping ratio of the oscillating mode under five different examples are given in Table 2.

As the real part of $\lambda_{2,3}$ enter into the right half plane of the S-plane in Example-2, Example-4, and Example-5, ξ changes into a negative and in the meanwhile gain margin (GM) and phase margin (PM) are both less than zero. Therefore, the system works in an unstable state at that time and the unstable phenomenon is represented by the low-frequency oscillation of the voltage and current.

Table 2. Eigenvalues, the damping ratio, and stability margin of the five sets examples of MPPT control parameters in simplified structure (SS).

Example	K_{p1}	T_{i1}	λ_1	$\lambda_{2,3}$	ξ	f_{os}/Hz	GM	PM	Stability
1	0.11	0.01	-80.12	$-163.96 \pm 2731.67i$	0.0599	434.76	+Inf	8.56°	Stable
2	0.11	0.001	-769.85	$180.90 \pm 2785.85i$	-0.0648	443.38	-15.2 dB	-9.42°	Unstable
3	0.05	0.01	-64.62	$-171.71 \pm 2047.13i$	0.0836	325.81	+Inf	14.8°	Stable
4	0.05	0.001	-623.17	$107.56 \pm 2089.24i$	-0.0514	332.51	-8.33 dB	-8.98°	Unstable
5	0.11	0.0068	-1072.42	$332.19 \pm 2849.09i$	-0.1158	453.45	-20.3 dB	-17.3°	Unstable

Remaining K_{p1} is unchanged at Example-1 and Example-2, it can be observed that the decreasing of T_{i1} will lead $\lambda_{2,3}$ move to the right half plane, which reduces the stability of the system. Let $T_{i1} = 0.01$ at Example-1 and Example-3, the increasing of K_{p1} causes $\lambda_{2,3}$ to move the right half plane and λ_1 to move to the left half plane. Besides, the PM of Example-1 and Example-3 are 8.56° and 14.8° respectively, which means that the stability in Example-3 is actually stronger than the stability in Example-1.

Along with practical application, it is usually found that one or several parameters have a dominant influence on a particular mode of the system, while other parameters take little or no impact. Since multiple circuit parameters exist on the converter, relative eigenvalue sensitivity is used here to evaluate the trajectory alteration when the system parameters changed [22].

To obtain the eigenvalue sensitivity, it is possible to screen for parameters that have an important influence on system stability. Let $\Phi = (\phi_1^T, \phi_2^T, \dots, \phi_n^T)^T$ be the left eigenmatrix of the state matrix \mathbf{A} , let $\Psi = (\psi_1, \psi_2, \dots, \psi_n)$ be the right eigenmatrix of the state matrix \mathbf{A} , and Λ be the diagonal matrix composed of the eigenvalues of the state matrix \mathbf{A} . Hence, their relationship can be expressed as

$$\begin{aligned} \Phi \mathbf{A} &= \Lambda \Phi \\ \mathbf{A} \Psi &= \Psi \Lambda \end{aligned} \tag{15}$$

Thus, the eigenvalue sensitivity can be defined as

$$RS_\alpha^{\lambda_i} = \lim_{\Delta\alpha \rightarrow 0} \frac{\Delta\lambda_i/\lambda_i}{\Delta\alpha/\alpha} = \frac{\alpha}{\lambda_i} \frac{\partial\lambda_i}{\partial\alpha} \tag{16}$$

where λ_i is the i th eigenvalue of the feature matrix \mathbf{A} , and α is a certain system parameter.

The first-order eigenvalue sensitivity of SS is given in Table 3 and it could be found that the sensitivity values of various parameters are significantly different due to the difference in parameter units. To address this problem, the concept of relative eigenvalue sensitivity is introduced to identify such differentiation between parameters.

Table 3. Eigenvalue sensitivity of different parameters in SS.

Parameters	S^{λ_1}	$S^{\lambda_{2,3}}$
C_{in}	208.7155	$618,063.1474 \pm 4,113,062.7390i$
L_b	-140.9152	$58.7597 \pm 687,790.4019i$
K_{p1}	-145.1916	$72.7656 \pm 9981.7933i$
T_{i1}	8033.2560	$-4016.6280 \pm 123.3540i$

It should be noted that the real part of the eigenvalue can clearly reflect the change of the state. For this reason, the relative eigenvalue sensitivity is defined only for the real part of the eigenvalue to simplify the analysis, and then Equation (16) can be replaced by

$$RS_{\alpha}^{\text{Re}(\lambda_i)} = \lim_{\Delta\alpha \rightarrow 0} \frac{\Delta\text{Re}(\lambda_i)/\text{Re}(\lambda_i)}{\Delta\alpha/\alpha} = \frac{\alpha}{\text{Re}(\lambda_i)} \frac{\partial\text{Re}(\lambda_i)}{\partial\alpha} \tag{17}$$

where $RS^{\text{Re}(\lambda_i)}$ reflects the impact of relative parameters changing.

Table 4 gives the relative eigenvalue sensitivity of the four key parameters of SS. Furthermore, Figures 4 and 5 depict the eigenvalue locus as the parameters changing. As shown in Table 4 and Figure 4, when $RS^{\text{Re}(\lambda_i)}$ is positive, eigenvalue locus moves toward the imaginary axis as the parameters increasing. And when $RS^{\text{Re}(\lambda_i)}$ is negative, eigenvalue locus moves away from the imaginary axis as the parameters increasing. From Figure 5a,b either T_{i1} is increasing or K_{p1} is decreasing, and the real part of λ_1 is increasing. However, the system is still stable, because the real eigenvalue is always less than 0. Furthermore, the reduction of T_{i1} and the increasing of C_{in} will make the real part of the oscillating mode $\lambda_{2,3}$ move from the left half plane into the right half plane shown in Figure 4a,c and Figure 5a,c. So, the system tends to be unstable along with the Hopf bifurcation. In addition, the effect of L_b on the stability of the system is almost negligible, which is consistent with the analysis of the relative eigenvalue sensitivity of L_b in Table 4.

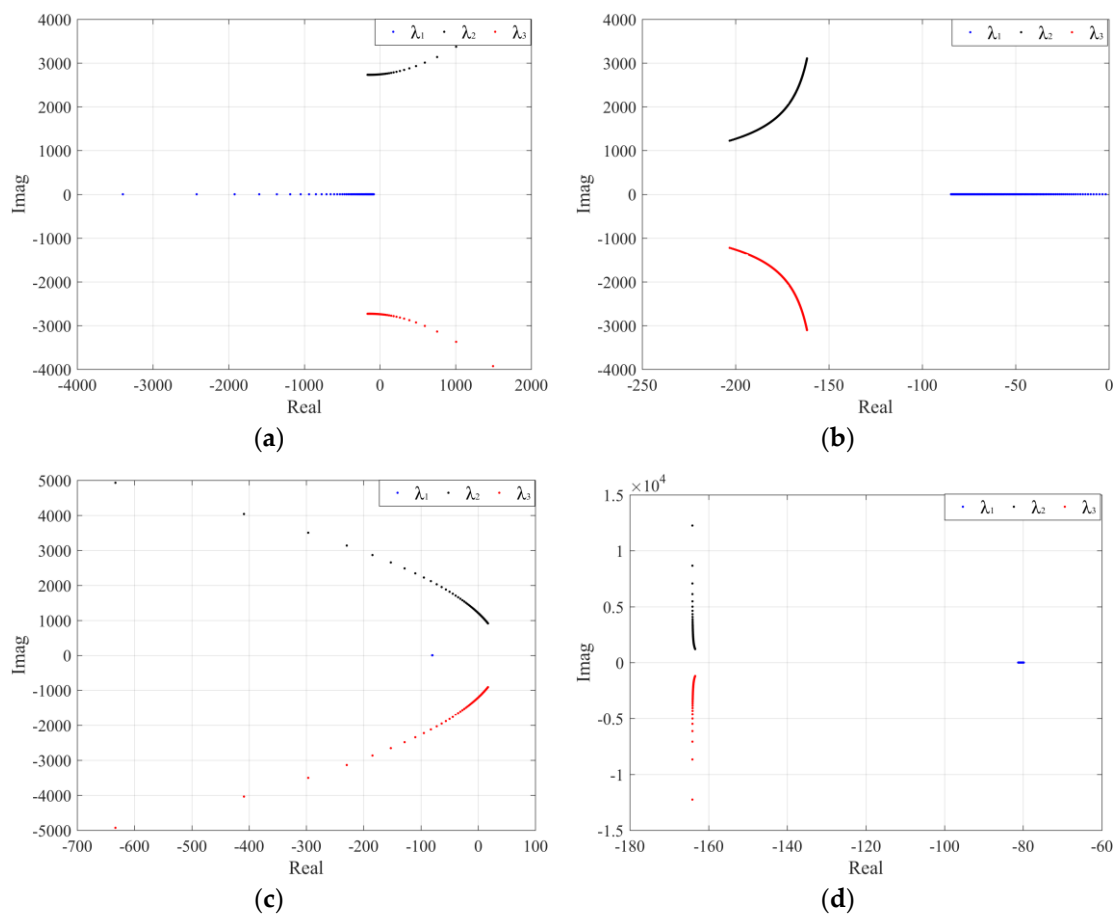


Figure 4. Loci of eigenvalue $\lambda_1, \lambda_2, \lambda_3$ as the changing of (a) T_{i1} ; (b) K_{p1} ; (c) C_{in} ; (d) L_b .

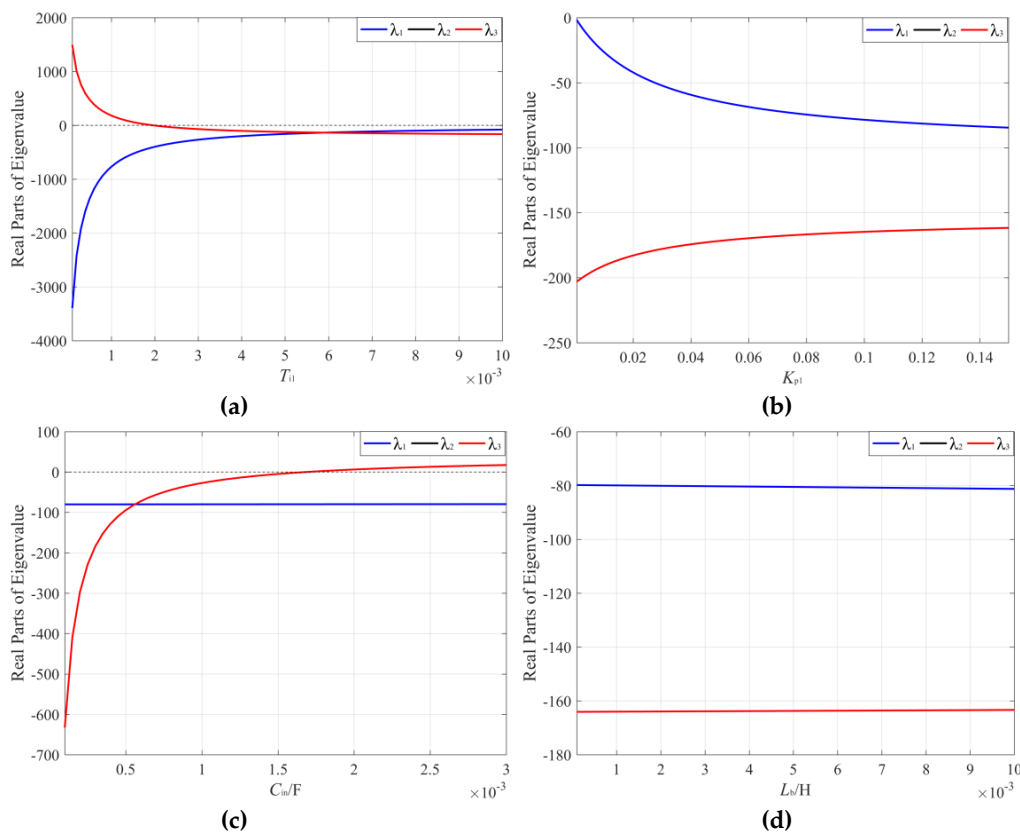


Figure 5. Trajectory of the real part of $\lambda_1, \lambda_2, \lambda_3$ as the changing of (a) T_{i1} ; (b) K_{p1} ; (c) C_{in} ; (d) L_b .

Table 4. Relative eigenvalue sensitivity of different parameters in SS.

Parameters	$RS^{Re}(\lambda_1)$	$RS^{Re}(\lambda_{2,3})$
C_{in}	0.00086	0.243054
L_b	-0.003518	0.000717
K_{p1}	-0.199342	-0.15669
T_{i1}	1.002668	-0.24497

4. Comparison of Stability Analysis between CS and SS

4.1. Stable Boundary

In this section, the model of PV grid-connected CS introduced in [20] is used, and then the stable boundary of SS and CS are compared. The parameters of the PV array and the converter are shown in Tables 1 and 5, respectively.

Table 5. Converter parameters.

Symbol	C_{in}	L_b	C_{dc}	L_f	C_f	f_s	U_{gm}
Quantity	330 μ F	2 mH	660 μ F	18 mH	0.5 μ F	20 kHz	17 V
Symbol	K_{p1}	T_{i1}	K_{p2}	T_{i2}	K_{p3}	T_{i3}	Z_g
Quantity	0.11	0.01	3.05	0.55	0.3	0.00014	0.2 Ω

Simulating the circuit of CS circuit, in which MPPT control parameters are assigned according to Example-2 and Example-4 shown in Table 2, respectively. The time domain waveform diagram of the PV voltage u_{pv} can be seen in Figure 6, and the corresponding fast fourier transform (FFT) analysis diagram is presented in Figure 7. A large peak amplitude appears at the low-frequency oscillation 422.9 Hz and 325.7 Hz of Example-2 and Example-4 respectively in Figure 7, which is roughly the

same as the calculated oscillation frequencies of 443.38 Hz and 332.51 Hz shown in Table 2. Therefore, consistent with the stability analysis of SS, low-frequency oscillation occurs in CS when the parameter in Example-2 and Example-4 are adopted. It indicates that the system is in an unstable state.

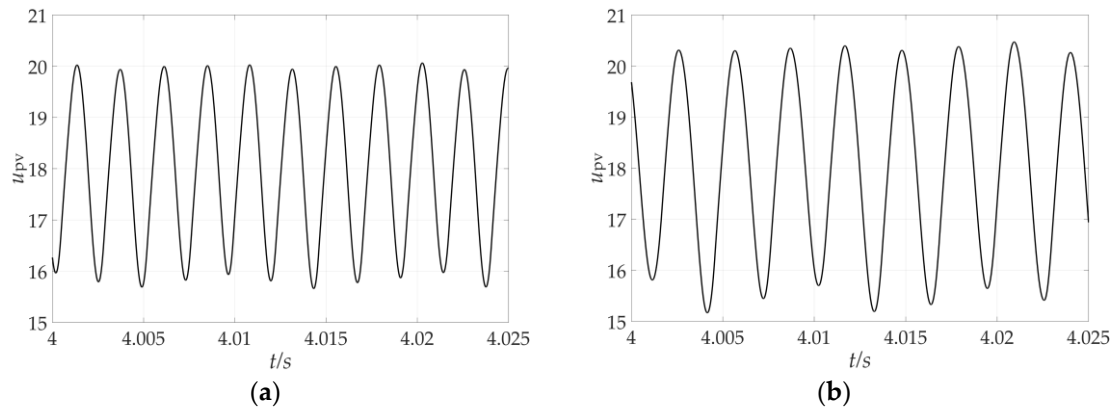


Figure 6. Waveform of u_{pv} when (a) $K_{p1} = 0.11, T_{i1} = 0.001$; (b) $K_{p1} = 0.05, T_{i1} = 0.001$.

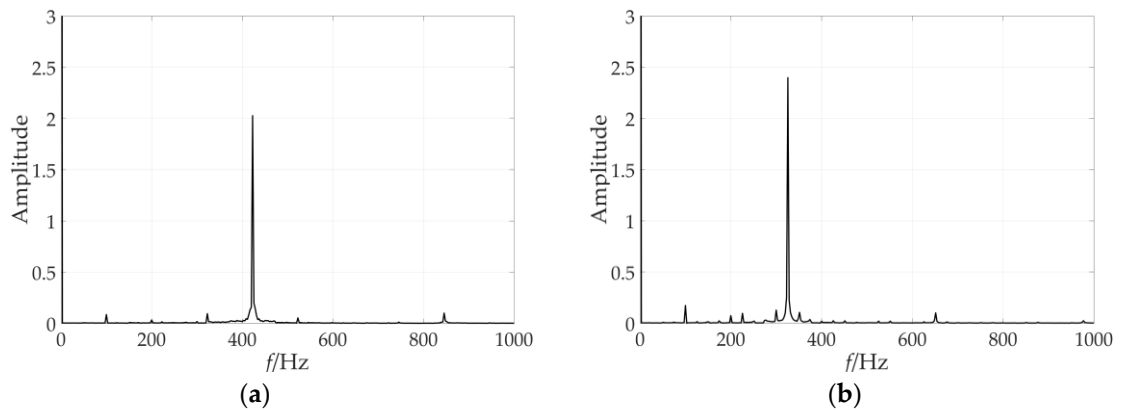


Figure 7. FFT spectrogram of u_{pv} when (a) $K_{p1} = 0.11, T_{i1} = 0.001$; (b) $K_{p1} = 0.05, T_{i1} = 0.001$.

Next, to further investigate the similarity of the stability of the two structures, Figure 8 depicts the stable boundary of SS and CS with respect to the parameter regions of K_{p1} and T_{i1} . It reveals that the almost same results of the stability analysis described in Section 3 are obtained. Besides, two parameter stability domains of SS are almost identical with CS, and just slight differences exist in the vicinity of the boundary. Thus, it can be concluded that the stability analysis of the dc-dc converter in CS can be carried out in SS.

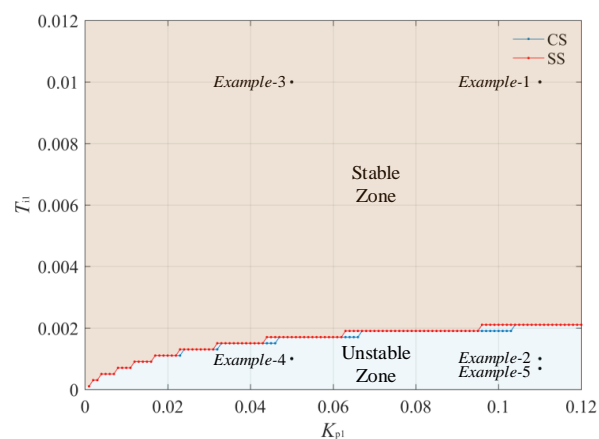


Figure 8. Comparison of stable boundary between SS and cascade structure (CS).

4.2. Connection and Distinction of SS and CS

According to the method mentioned in Section 3, the relative eigenvalue sensitivity of CS is obtained in Table 6.

Table 6. Relative eigenvalue sensitivity of different parameters in CS ¹.

Area	Symbol	RS ^{Re(λ1)}	RS ^{Re(λ2,3)}	RS ^{Re(λ4,5)}	RS ^{Re(λ6,7)}	RS ^{Re(λ8)}	RS ^{Re(λ9)}	RS ^{Re(λ10,11)}
Circuit Parameters	<i>C_{in}</i>	0.000642	-6.758×10^{-10}	-6.833×10^{-9}	0.001866	0.000753	5.344×10^{-8}	0
	<i>L_b</i>	-0.000646	-0.000002	-0.000004	0.000887	-0.003511	-4.277×10^{-9}	0
	<i>C_{dc}</i>	0.184256	0.000447	0.000637	9.482×10^{-7}	2.860×10^{-7}	-0.000091	0
	<i>L_f</i>	0.112214	0.094583	0.006227	0.000002	1.354×10^{-8}	-0.000003	0
	<i>K_{p1}</i>	-0.000531	-7.825×10^{-9}	7.870×10^{-9}	-0.000604	-0.199416	0.000040	0
Control Parameters	<i>T_{i1}</i>	-0.000012	1.23193×10^{-9}	-3.270×10^{-9}	-0.000896	1.002759	-0.000004	0
	<i>K_{p2}</i>	-0.337422	-0.000387	-0.000517	0.000074	-0.000007	-0.000356	0
	<i>T_{i2}</i>	-0.000136	-1.249×10^{-7}	-0.000002	3.270×10^{-8}	-0.000002	1.000161	0
	<i>K_{p3}</i>	-0.263605	0.000879	-0.001749	0.000001	-5.129×10^{-9}	-0.000438	0
	<i>T_{i3}</i>	0.704758	-0.000053	-0.006086	-0.000005	-3.708×10^{-8}	0.000945	0

¹ The bold sections represent the main key data.

From Table 6, its influence on different oscillation modes is different for one parameter. For example, the most influential parameter of oscillation mode $\lambda_{6,7}$ is *C_{in}*, *K_{p1}*, and *T_{i1}* have the greatest influence on the attenuation mode λ_8 . Compared with Table 4, it can be found that λ_8 and $\lambda_{6,7}$ in CS are analogous to λ_1 and $\lambda_{2,3}$ in SS, respectively. So, it means the performance of *C_{in}*, *K_{p1}*, and *T_{i1}* are almost identical in the two structures.

In the small disturbance analysis method, the eigenvalue analysis can judge the stability of the system. However, the eigenvalue is based on the analysis performed at steady-state. To analyze the correlation between the state variables of SS and CS under the transient condition after the disturbance completed, the modal participation factor of the state variable is introduced.

According to the nature of the eigenvalues, each eigenvalue corresponds to a modality of the system. The real eigenvalue corresponds to the attenuation mode of the system, and the conjugate complex eigenvalue corresponds to the oscillating mode. Among the basic modal listed in Table 6, there are three attenuation modes λ_1 , λ_8 , and λ_9 and four oscillation modes $\lambda_{2,3}$, $\lambda_{4,5}$, $\lambda_{6,7}$, and $\lambda_{10,11}$, which play a decisive role in the dynamic behavior of the system. In addition, $\lambda_{10,11}$ is independent of the stability of the system due to the introduction of virtual state variables, and it is also independent of the inherent characteristics of the system.

The modal participation factor is a measure that combines the left and right eigenvectors as the degree of interaction between the state variables and the modalities. The correlation between the *k*th state variable to the *i*th mode can be represented by a modal participation factor [30] as follows

$$P_{ki} = \phi_{ik}\psi_{ki} \tag{18}$$

where ϕ_{ik} represents the *k*th element of the row vector ϕ_i ; ψ_{ki} represents the *k*th element of the column vector ψ_i . P_{ki} describes the scale of the effect of the *i*th mode and the *k*th state variable in the case of the *k*th state variable is under unit perturbation.

Equation (18) indicates that the modal participation factor is only related to the structural parameters of the system. And it has nothing to do with the disturbance, which is similar to the property of the sensitivity of the eigenvalue. The modal participation factors of the system are given in Table 7. It can be seen clearly that the attenuation mode λ_1 is mainly related to the voltage deviation signal *u_e* of the voltage outer loop, the oscillation modes $\lambda_{2,3}$ and $\lambda_{4,5}$ are mainly related to *i_o* and *u_{c2}*, the oscillation mode $\lambda_{6,7}$ is mainly related to *i_{Lb}* and *u_{c1}*, the attenuation mode λ_8 is mainly related to *u_{Cin}* and *u_{c1}*, the attenuation mode λ_9 is mainly related to *u_{dc}*, and the undamped oscillation mode $\lambda_{10,11}$ is only related to the constructed virtual state variables *g₁* and *g₂*. According to the modal participation factor of the system, the basic mode closely related to a certain state variable of the system can be known, thereby a certain state of the system can be affected by regulating the basic mode. Additionally,

the nonlinear interaction between the front-stage dc-dc converter and the rear-stage dc-ac inverter can be found through modal participation factor. In Table 7, the corresponding three state variables of SS are u_{Cin} , i_{Lb} , and u_{c1} . Based on the above analysis, u_{Cin} , i_{Lb} , and u_{c1} are the main state variables affecting $\lambda_{6,7}$ and λ_8 . However, they also play almost no effect on the other modes, which indicates that parameters of the front-stage converter designed by SS will not adversely affect the rear-stage inverter in CS.

Table 7. Modal participation factors of state variables in CS ¹.

PF	λ_1	$\lambda_{2,3}$	$\lambda_{4,5}$	$\lambda_{6,7}$	λ_8	λ_9	$\lambda_{10,11}$
u_{Cin}	0.000099	1.695×10^{-8}	0.000005	0.097897	0.804096	1.588×10^{-8}	0
i_{Lb}	0.000646	0.000004	0.000476	0.501598	0.003511	3.979×10^{-9}	0
u_{c1}	0.000531	0.000001	0.000008	0.400021	0.199416	0.000004	0
u_{dc}	0.153302	0.000275	0.075594	0.000954	0.000071	0.999728	0
i_{od}	0.000211	0.498952	0.000944	0.000002	4.491×10^{-10}	1.293×10^{-7}	0
i_{oq}	0.020693	0.000568	0.509190	0.000589	7.752×10^{-7}	2.383×10^{-8}	0
u_e	0.911923	0.00181	0.043321	0.001300	0.000071	0.000343	0
u_{c2d}	0.000104	0.499432	0.000514	0.000002	2.013×10^{-9}	1.121×10^{-9}	0
u_{c2q}	0.261774	0.001041	0.369947	0.000240	2.251×10^{-7}	0.000067	0
g_1	0	0	0	0	0	0	0.5
g_2	0	0	0	0	0	0	0.5

¹ The bold sections represent the main key data.

5. Experiment Verification

To experimentally evaluate the consistency of the stability analysis of the PV system in SS, an experimental setup is implemented as shown in Figure 9. The parameters are consistent with Tables 1 and 5.

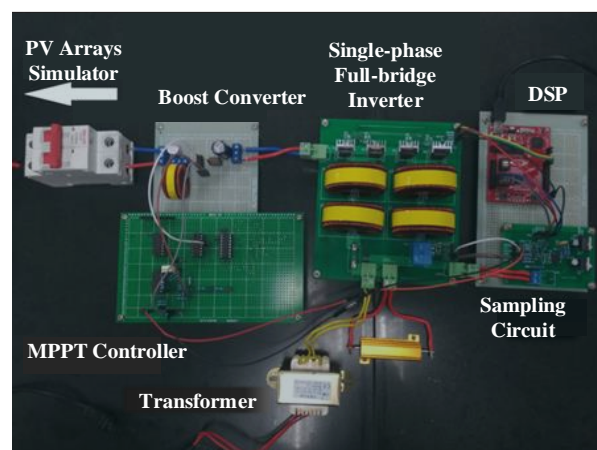


Figure 9. Experimental setup.

The PV analog power supply uses the Chroma programmable dc current supply 62150H- 1000S. The input capacitor C_{in} is Panasonic's 25SEPF330M. The diode VD is General Semiconductor's FES8JT. The drive power supply uses the IR2101 chip. In the control circuit of the dc-dc converter, the amplifier used a four-channel LM324AD, and the comparator uses a four-channel LM2901. In the dual-loop control of single-phase full-bridge inverter, it is achieved by using the TMS320F28027 micro-processor. The output current is sampled by a WCS2705 Hall sensor. Furthermore, the grid voltage and dc bus voltage sampling circuit are sampled by differential amplifier circuit, and the amplifier adopts TLV2374.

We first investigated what happens when the corresponding circuit of CS is applied. Figure 10 gives a description of the experimental waveform and FFT analysis results of u_{dc} in CS under the two

sets of MPPT parameters. When $K_{p1} = 0.11$ and $T_{i1} = 0.01$ shown in Figure 10a, the u_{dc} waveform approximates a complete sine wave. And the peak voltage appears only at the fundamental frequency multipliers of 100 Hz and 200 Hz in the FFT spectrum, therefore, the system is in a stable state. When $K_{p1} = 0.11$ and $T_{i1} = 0.00068$, u_{dc} has a certain degree of distortion, and its FFT spectrum shows a peak at 450 Hz in Figure 10b. The system shows an unstable oscillation phenomenon.

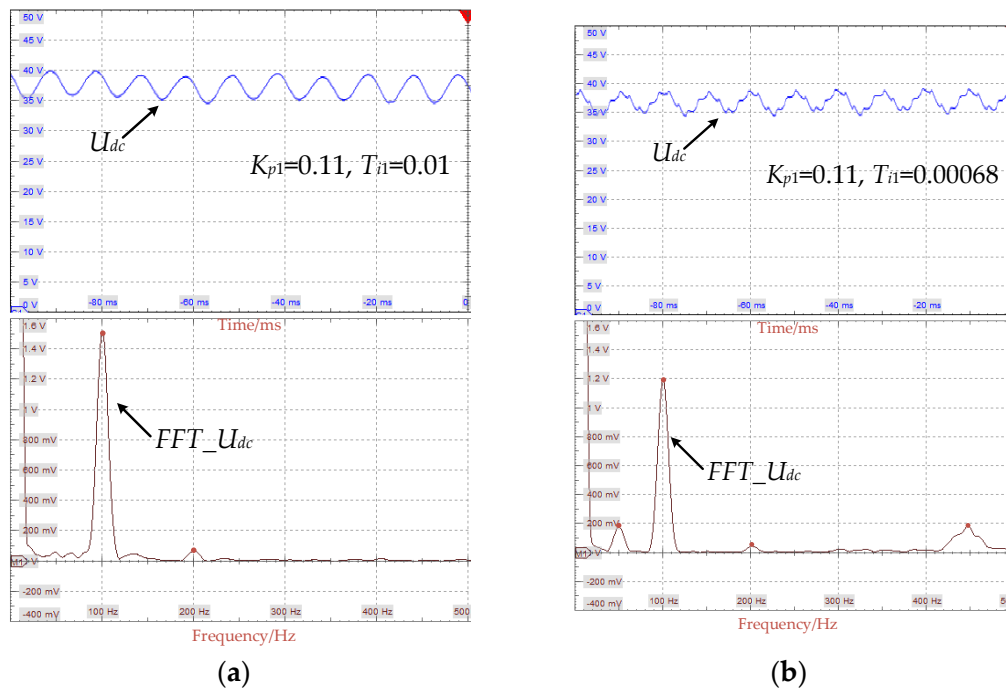


Figure 10. Experimental waveform and FFT analysis results of dc bus voltage u_{dc} in CS at (a) $[K_{p1}, T_{i1}] = [0.11, 0.01]$; (b) $[K_{p1}, T_{i1}] = [0.11, 0.00068]$.

Next, we try to find a similar performance when the Boost converter is worked alone. Figure 11 illustrates the experimental waveform and FFT analysis of u_{pv} in SS from the three sets of MPPT control parameters. When $K_{p1} = 0.11$ and $T_{i1} = 0.01$, u_{pv} is basically going to keep the voltage at the maximum power point as shown in Figure 11a. When $K_{p1} = 0.11$ and $T_{i1} = 0.001$, u_{pv} exhibits a small oscillation. It can be seen from the FFT diagram of Figure 11b that there is an intermediate frequency oscillation about at 530 Hz. When $K_{p1} = 0.11$ and $T_{i1} = 0.00068$, as shown in Figure 11c, the voltage waveform appears more severely distorted for the oscillation amplitude is increased, and a medium-frequency oscillation nearly appears at 420 Hz. Thus, the system becomes unstable.

Comparing Figure 10 with Figure 11, we obtained the same stability analysis results when the two structures operate in the same MPPT parameters. It is in accordance with the description of stable boundary from Section 4. Additionally, the oscillation frequencies of Figure 11b,c are substantially the same as those of the theoretical values obtained in Table 2. Consequently, the consequences obtained in the earlier sections are validated in the experiments.

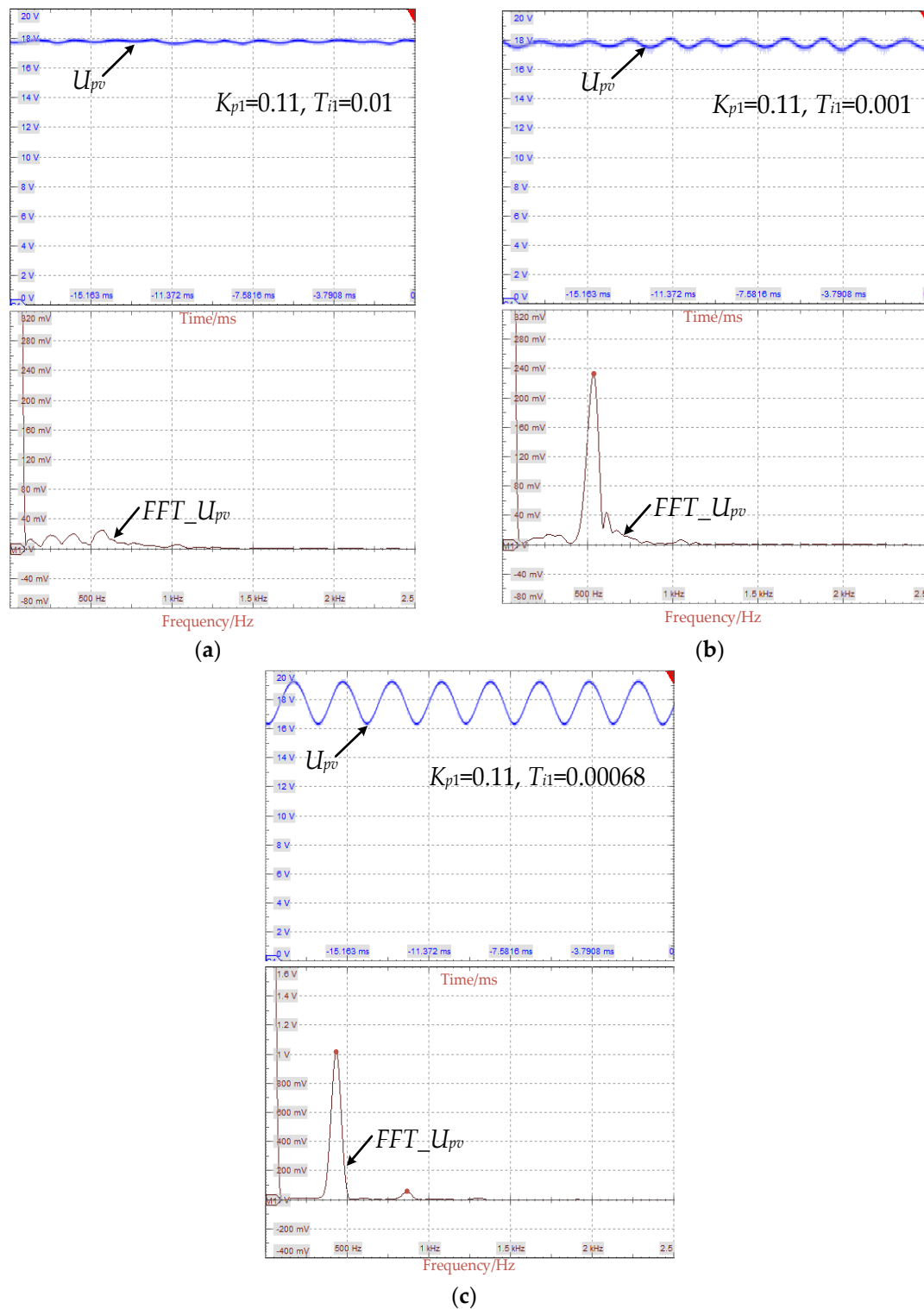


Figure 11. Experimental waveform and FFT analysis results of PV array output voltage u_{pv} in SS at (a) $[K_{p1}, T_{i1}] = [0.11, 0.01]$; (b) $[K_{p1}, T_{i1}] = [0.11, 0.001]$; (c) $[K_{p1}, T_{i1}] = [0.11, 0.00068]$.

6. Conclusions

For two-stage PV system, this research uses SS instead of CS to simplify the parameter design of the front-stage dc-dc converter, which can avoid the influence of the parameter coupling in CS. To linearize the nonlinear characteristics of the output current and output voltage in PV array, the average model of SS is established by small-signal analysis method, and, further, the eigenvalue matrix

is obtained. Relative eigenvalue sensitivity measure indicates that K_{p1} , T_{i1} , C_{in} , and L_b of the dc-dc converter can exert the equally major effect on one oscillating mode and one attenuating mode in SS and CS. It is also verified through damping ratio and root-locus analysis. By curving the stability boundaries of MPPT controller parameters K_{p1} and T_{i1} in the aforementioned two structures, the comparison of the two broken-line shows that they have approximate stability domains, and five sets of MPPT examples analyzed in the two structures have the similar stability, which further validates the feasibility of SS instead of CS to design the front-stage dc-dc converter. Furthermore, the modal participation factor is used to describe the interaction between SS and CS. It shows the mode related to the parameters in dc-dc converter is hardly affected by other parts of two-stage PV system. Finally, two sets of MPPT examples tested in CS and three sets of MPPT examples tested in SS perform show almost identical stability, and it is also in accordance with the analysis above in the oscillation frequency. All of which point toward the conclusion that, in two-stage PV system with dc bus, the simplified structure can be used to replace the cascade structure for parameter design optimization of the dc-dc converter.

Author Contributions: Conceptualization, F.X.; Formal analysis, Z.L.; Investigation, L.H.; Methodology, D.Q. and L.H.; Validation, Z.L.; Writing—original draft, Z.L.; Writing—review & editing, F.X., D.Q., B.Z. and Y.C.

Funding: This research was funded by the Key Program of National Natural Science Foundation of China, grant number 2018YFB0905804, the Team Program of Natural Science Foundation of Guangdong Province, China, grant number 2017B030312001, and the National Natural Science Foundation of China, grant number 51507068.

Conflicts of Interest: The authors declare no conflict of interest.

References

1. Kjaer, S.B.; Pedersen, J.K.; Blaabjerg, F. A review of single-phase grid-connected inverters for photovoltaic modules. *IEEE Trans. Ind. Appl.* **2005**, *41*, 1292–1306. [[CrossRef](#)]
2. Pandey, A.K.; Tyagi, V.V.; Selvaraj, J.A.L.; Rahim, N.A.; Tyagi, S.K. Recent advances in solar photovoltaic systems for emerging trends and advanced applications. *Renew. Sustain. Energy Rev.* **2016**, *53*, 859–884. [[CrossRef](#)]
3. Li, Q.; Wolfs, P. A review of the single phase photovoltaic module integrated converter topologies with three different DC link configurations. *IEEE Trans. Power Electron.* **2008**, *23*, 1320–1333.
4. Darwish, A.; Massoud, A.M.; Holliday, D.; Ahmed, S.; Williams, B.W. Single-stage three-phase differential-mode buck-boost inverters with continuous input current for PV applications. *IEEE Trans. Power Electron.* **2016**, *31*, 8218–8236. [[CrossRef](#)]
5. Haroun, R.; Aroudi, A.E.; Cid-Pastor, A.; Garcia, G.; Olalla, C.; Martinez-Salamero, L. Impedance matching in photovoltaic systems using cascaded Boost converters and sliding-mode control. *IEEE Trans. Power Electron.* **2015**, *30*, 3185–3199. [[CrossRef](#)]
6. Martins, D.C.; Demonti, R. Photovoltaic energy processing for utility connected system. In Proceedings of the 27th Annual Conference of the IEEE Industrial-Electronics-Society, Denver, CO, USA, 29 November–2 December 2001; Volume 1–3.
7. Prapanavarat, C.; Barnes, M.; Jenkins, N. Investigation of the performance of a photovoltaic AC module. *Proc. IEE Gener. Transm. Distrib.* **2002**, *149*, 472–478. [[CrossRef](#)]
8. Al-Hindawi, M.M.; Abusorrah, A.; Al-Turki, Y.; Giaouris, D.; Mandal, K.; Banerjee, S. Nonlinear dynamics and bifurcation analysis of a boost converter for battery charging in photovoltaic applications. *Int. J. Bifurc. Chaos* **2014**, *24*, 373–491. [[CrossRef](#)]
9. Zhioua, M.; Aroudi, A.E.; Belghith, S.; Bosque-Moncusí, J.M.; Giral, R.; Al Hosani, K.; Al-Numay, M. Modeling, dynamics, bifurcation behavior and stability analysis of a DC–DC boost converter in photovoltaic systems. *Int. J. Bifurc. Chaos* **2016**, *26*, 458–471. [[CrossRef](#)]
10. Huang, M.; Ji, H.; Sun, J.; Wei, L.; Zha, X. Bifurcation based stability analysis of photovoltaic-battery hybrid power system. *IEEE J. Emerg. Sel. Top. Power Electron.* **2017**, *5*, 1055–1067. [[CrossRef](#)]
11. Wang, L.; Lin, Y.H. Small-signal stability and transient analysis of an autonomous PV system. In Proceedings of the IEEE/PES Transmission & Distribution Conference & Exposition, Chicago, IL, USA, 21–24 April 2008.
12. Ge, J.; Du, H.; Zhao, D.; Ma, J.; Qian, M.; Zhu, L. Influences of grid-connected photovoltaic power plants on low frequency oscillation of multi-machine power systems. *Autom. Electr. Power Syst.* **2016**, *40*, 63–70.

13. Gao, B.; Yao, L.; Li, R. Analysis on oscillation modes of large-scale grid-connected PV power plant. *Electr. Power Autom. Equip.* **2017**, *37*, 123–130.
14. Tse, K.K.; Ho, M.T.; Chung, H.S.H.; Hui, S.Y. A novel maximum power point tracker for pv panels using switching frequency modulation. *IEEE Trans. Power Electron.* **2002**, *17*, 980–989. [[CrossRef](#)]
15. Koutroulis, E.; Kalaitzakis, K.; Voulgaris, N.C. Development of a microcontroller-based, photovoltaic maximum power point tracking control system. *IEEE Trans. Power Electron.* **2001**, *16*, 46–54. [[CrossRef](#)]
16. Sreekanth, T.; Lakshminarasamma, N.; Mishra, M.K. A Single-stage grid-connected high gain buck-boost inverter with maximum power point tracking. *IEEE Trans. Energy Convers.* **2017**, *32*, 330–339. [[CrossRef](#)]
17. Saublet, L.M.; Gavagsaz-Ghoachani, R.; Martin, J.P.; Nahid-Mobarakeh, B.; Pierfederici, S. Asymptotic stability analysis of the limit cycle of a cascaded DC–DC converter using sampled discrete-time modeling. *IEEE Trans. Ind. Electron.* **2016**, *63*, 2477–2487. [[CrossRef](#)]
18. Zadeh, M.K.; Gavagsaz-Ghoachani, R.; Pierfederici, S.; Nahid-Mobarakeh, B.; Pierfederici, S. Stability analysis and dynamic performance evaluation of a power electronics-based DC distribution system with active stabilizer. *IEEE J. Emerg. Sel. Top. Power Electron.* **2016**, *4*, 93–102. [[CrossRef](#)]
19. Xie, F.; Zhang, B.; Qiu, D.; Jiang, Y. Non-linear dynamic behaviours of DC cascaded converters system with multi-load converters. *IET Power Electron.* **2016**, *9*, 1093–1102. [[CrossRef](#)]
20. Huang, L.; Qiu, D.; Xie, F.; Chen, Y.; Zhang, B. Modeling and stability analysis of a single-phase two-stage grid-connected photovoltaic system. *Energies* **2017**, *10*, 2176. [[CrossRef](#)]
21. Aroudi, A.E.; Giaouris, D.; Mandal, K.; Banerjee, S.; Al-Hindawi, M.; Abusorrah, A.; Al-Turki, Y. Complex nonlinear phenomena and stability analysis of interconnected power converters used in distributed power systems. *IET Power Electron.* **2016**, *9*, 855–863. [[CrossRef](#)]
22. Figueres, E.; Garcera, G.; Sandia, J.; Gonzalez-Espin, F.; Rubio, J.C. Sensitivity study of the dynamics of three-phase photovoltaic inverters with an LCL grid filter. *IEEE Trans. Ind. Electron.* **2009**, *56*, 706–717. [[CrossRef](#)]
23. Moradi-Shahrbabak, Z.; Tabesh, A. Effects of front-end converter and DC-link of a utility-scale PV energy system on dynamic stability of a power system. *IEEE Trans. Ind. Electron.* **2018**, *65*, 403–411. [[CrossRef](#)]
24. Yang, S.; Lei, Q.; Peng, F.; Qian, Z. A robust control scheme for grid-connected voltage-source inverters. *IEEE Trans. Ind. Electron.* **2011**, *58*, 202–212. [[CrossRef](#)]
25. Ouyang, Y.; Zou, Y. Static stability analysis of outer-loop control in grid-connected inverters under weak grid condition. In Proceedings of the International Conference on Power System Technology (POWERCON), Guangzhou, China, 6–8 November 2018.
26. Viinamäki, J.; Jokipii, J.; Messo, T.; Suntio, T.; Sitbon, M.; Kuperman, A. Comprehensive dynamic analysis of photovoltaic generator interfacing DC–DC boost power stage. *IET Renew. Power Gener.* **2015**, *9*, 306–314. [[CrossRef](#)]
27. Khouzam, K.; Cuong, L.; Chen, K.K.; Poo, Y.N. Simulation and real-time modelling of space photovoltaic systems. In Proceedings of the IEEE 1st World Conference on Photovoltaic Energy Conversion, Waikoloa, HI, USA, 5–9 December 1994; Volume 2, pp. 2038–2041.
28. Hung, M.F.; Tseng, K.H. Study on the corresponding relationship between dynamics system and system structural configurations-Develop a universal analysis method for eliminating the RHP-zeros of system. *IEEE Trans. Ind. Electron.* **2018**, *65*, 5774–5784. [[CrossRef](#)]
29. Gao, F.; Li, D.; Loh, P.C.; Tang, Y.; Wang, P. Indirect dc-link voltage control of two-stage single-phase PV inverter. In Proceedings of the IEEE Energy Conversion Congress and Exposition, San Jose, CA, USA, 20–24 September 2009; pp. 1166–1172.
30. Yazdani, A.; Dash, P.P. A control methodology and characterization of dynamics for a photovoltaic (PV) system interfaced with a distribution network. *IEEE Trans. Power Deliv.* **2009**, *24*, 1538–1551. [[CrossRef](#)]

